Applied Radiation and Isotopes 226 (2025) 112143

Contents lists available at ScienceDirect

Applied Radiation and Isotopes

journal homepage: www.elsevier.com/locate/apradiso

Laser photo-ionization efficiency of ^{111}Ag for medical use in the SPES-ISOLPHARM project

Alberto Arzenton [a,b,*], Emilio Mariotti [a,c,*], Daniele Scarpa [b], Omorjit Singh Khwairakpam [b], Piergiorgio Nicolosi [d], Davide Serafini [a,b], Leonardo Mariotti [a], Alberto Andrighetto [b]

[a] University of Siena, Department of Physical Sciences, Earth and Environment, Via Roma 56, 53100, Siena, Italy
[b] INFN, Legnaro National Laboratories, Viale dell'Università 2, Legnaro, 35020, Italy
[c] INFN, Pisa Division, Via F. Buonarroti 3, Pisa, 56127, Italy
[d] Senior Scholar, University of Padova, Via VIII Febbraio 2, Padova, 35122, Italy

ARTICLE INFO

Keywords:
Laser
Photo-ionization
Radionuclide production
Silver-111
Density matrix
ISOL
SPES-ISOLPHARM

ABSTRACT

The ISOLPHARM project has the goal of producing innovative radiopharmaceuticals taking advantage of the radionuclides produced in the SPES ISOL facility, nearing completion at INFN-LNL. One of the main radionuclides of interest for the project is ^{111}Ag, which is a novel candidate for therapeutic and theranostic applications in nuclear medicine. Among the various steps of the ISOL technique, which stands for "Isotope Separation On-Line", the main stages contributing to selectivity are ionization and mass separation. In general, the latter ensures isotopic selectivity, while the former can be element-specific. In particular, the Laser Ion Source (LIS) is the one that guarantees the best selectivity, as it can provide to each element the precise energy required for ionization. Moreover, if narrowband lasers are available, the isotopic shift in one of the ionization steps can be used to tell apart different isotopes as well. The aim of this study is to assess, through the formalism of the reduced density matrix, the optimum laser power to maximize the ion yield and the isotopic selectivity of ^{111}Ag in the SPES online environment. Furthermore, other aspects affecting the yield, such as time delay, power broadening and Doppler broadening, are evaluated.

1. Introduction

The ISOLPHARM project (Vettorato et al., 2022; Andrighetto et al., 2019), headed by the Legnaro National Laboratories (LNL) of the Italian National Institute for Nuclear Physics (INFN), has been conceived in 2014 with the aim of producing innovative radiopharmaceuticals using the nuclides produced by Isotope Separation On-Line (ISOL) in the "SPES" facility. Up to the present day, the project has involved several Italian and international institutions, including universities and hospitals, united by a strong interest in the silver isotope ^{111}Ag. This radionuclide, thanks to its β^- and γ decay radiations and to its suitable half-life ($\sim$ 7.45 d), is considered a possible candidate for therapeutic and theranostic approaches in nuclear medicine. Several studies about ^{111}Ag have been conducted in the first 10 years of ISOLPHARM to investigate its ISOL production (Ballan et al., 2021), chemical purification and chelation (Tosato et al., 2020; Tosato and Asti, 2023), dosimetry (Arzenton et al., 2022), radiobiology (Arzenton, 2023) and imaging features (Serafini et al., 2025). The ISOL technique, if a uranium carbide (UC_x) target is employed, is one of the best ways to produce this radionuclide *carrier-free*, namely without isotopic contaminants. Production in nuclear reactors is also available (Morselli et al., 2023), but with a few important disadvantages: the low production yield, the high cost of enriched ^{110}Pd targets and the difficult chemical separation from palladium itself.

In general, the typical activity required for a single patient in β^- therapy is a few GBq, as in the case of ^{177}Lu-based drugs (EMA, 2022); relying on calculations performed in previous works (Arzenton, 2019), the ISOL technique at SPES is believed to be able to produce $\sim$ 1 GBq of ^{111}Ag in an irradiation cycle of 6 h using a 40 MeV proton beam with 200 μA intensity. Provided the long half-life of the nuclide (7.45 d), multiple cycles could easily obtain the desired activity. Anyway, the medical use of ^{111}Ag is still in the preclinical phase, where experiments on cells and small animals require much less activity than in human patients. The radionuclidic purity required can change according to the particular radiopharmaceutical, but usually values from 99.0% to

* Corresponding authors at: University of Siena, Department of Physical Sciences, Earth and Environment, Via Roma 56, 53100, Siena, Italy.
E-mail addresses: alberto.arzenton@unisi.it (A. Arzenton), emilio.mariotti@unisi.it (E. Mariotti), daniele.scarpa@lnl.infn.it (D. Scarpa), omorjit.khwairakpam@lnl.infn.it (O.S. Khwairakpam), piergiorgio.nicolosi@unipd.it (P. Nicolosi), davide.serafini@lnl.infn.it (D. Serafini), l.mariotti5@student.unisi.it (L. Mariotti), alberto.andrighetto@lnl.infn.it (A. Andrighetto).

https://doi.org/10.1016/j.apradiso.2025.112143
Received 9 January 2025; Received in revised form 7 August 2025; Accepted 27 August 2025
Available online 2 September 2025
0969-8043/© 2025 The Authors. Published by Elsevier Ltd. This is an open access article under the CC BY license (http://creativecommons.org/licenses/by/4.0/).

99.9% are required (Balzer et al., 2023). With the ISOL technique, these values can generally be obtained with mass separators. At SPES, a low-resolution mass separation system is installed; this includes a Wien filter with nominal resolution $\Delta M/M \sim 1/150$ plus a magnetic dipole and a series of electrostatic elements estimated to improve the resolution up to about $\Delta M/M \sim 1/200$ (Gramegna and the SPES collaboration, 2019). These values, if confirmed experimentally for heavy ions, can in theory allow to exclude 99.9% of isotopic contaminants; however, if the contaminants decay faster than the desired nuclide (and thus have a higher activity per mass unit), overcoming the threshold is not straightforward.

In the context of ISOL production at SPES, ion sources represent a fundamental aspect, enabling the extraction of exotic isotopes produced in the form of radioactive ion beams. The Laser Ion Source (LIS) is definitely the most selective one, since it takes advantage of the quantum nature of the atomic excitation. In a nutshell, the working principle is such that a set of laser beams whose photon frequencies are tuned on resonant energy jumps can push the most external electron close to the ionization threshold, or even over it, via stepwise population of a few excited states of the atoms of interest. In this way, if the laser bandwidths are sufficiently narrow, only the desired element is ionized. Furthermore, for very narrow bandwidths, it is sometimes possible to exploit the hyperfine splitting of certain levels and discriminate between different isotopes, even if the Doppler effect as well as other line-broadening mechanisms are able to kill this very high selectivity. Anyway, one has to take into account that typically the ISOL technique already includes mass separation as one of the last steps. Regarding the SPES LIS, its structure, mechanics, thermal properties and performance characterization have been exhaustively described elsewhere (Scarpa et al., 2022; Khwairakpam et al., 2024a,b).

Dealing with silver, the SPES laser group managed an offline experimental campaign to study two ionization schemes suitable for the online Ti:Sa laser systems. The schemes start from the ground state and are based on two resonant steps, favored by two different lasers, plus a non-resonant ionization step induced by a photon coming from one of the two beams:

1. $4d^{10}5s\ {}^2S_{1/2} \xrightarrow{328.163\,\text{nm}} 4d^{10}5p\ {}^2P^o_{3/2} \xrightarrow{421.217\,\text{nm}} 4d^{10}6d\ {}^2D_{5/2} \xrightarrow{\text{non-res.}} Ag^+$;
2. $4d^{10}5s\ {}^2S_{1/2} \xrightarrow{328.163\,\text{nm}} 4d^{10}5p\ {}^2P^o_{3/2} \xrightarrow{421.402\,\text{nm}} 4d^{10}6d\ {}^2D_{3/2} \xrightarrow{\text{non-res.}} Ag^+$.

The first path was studied in a Hollow Cathode Lamp (HCL) (Khwairakpam et al., 2022), whereas the second was evaluated in an atomic plume created by a high-power ablation laser on a silver target (Khwairakpam et al., 2023). Both configurations used a mixture of stable natural silver, composed by 51.839% ^{107}Ag and 48.161% ^{109}Ag. As also visible in Fig. 1, the main difference between the two paths is represented by the fine-structure level chosen for the second excitation step: $J = 5/2$ for scheme 1, $J = 3/2$ for scheme 2. Moreover, the latter has a lower but not negligible probability of decaying to a non-resonant level at 29 552 cm^{-1}, which then re-populates the ground state.

In the present study, these two schemes are evaluated by means of the reduced density matrix (see below). In particular, the ion yield attainable with the SPES offline and online laser devices is investigated as a function of the average power of each laser, taking also into account the time delay between the laser pulses and the possible broadening effects. Finally, a few considerations on isotopic selectivity are provided.

2. Theory

The system dynamics of a population of atoms getting excited and ionized by a laser pulse can be precisely modeled by quantum mechanics using the density operator, identified by the homonymous matrix, which can describe the time evolution of statistical mixtures of quantum states (Shore, 1990; Haken et al., 1965). Many applications of this formalism to the laser photo-ionization of exotic radionuclides can be found in the literature (Suryanarayana and Sankari, 2023; Sankari et al., 2008; Suryanarayana, 2021, 2022, 2023; Kiran Kumar et al., 2003). The diagonal elements of the reduced density matrix represent the atomic populations; in this case, five populations are considered: ground state, 1st excited level, 2nd excited level, non-resonant level (only scheme 2) and ion state. The equations describing their time derivatives are respectively:

$$\begin{aligned}
\dot\rho_{11}(t) &= -\frac{i}{2}\Omega_{21}(t)\cdot\rho_{12}(t) + \frac{i}{2}\Omega_{12}(t)\cdot\rho_{21}(t) + 2\big(A_{21}\cdot\rho_{22}(t) + A_{41}\\
&\quad\cdot\rho_{44}(t)\big),\\
\dot\rho_{22}(t) &= -\frac{i}{2}\Omega_{12}(t)\cdot\rho_{21}(t) + \frac{i}{2}\Omega_{21}(t)\cdot\rho_{12}(t) - \frac{i}{2}\Omega_{32}(t)\cdot\rho_{23}(t)\\
&\quad + \frac{i}{2}\Omega_{23}(t)\cdot\rho_{32}(t) + 2A_{32}\cdot\rho_{33}(t) - 2A_{21}\cdot\rho_{22}(t),\\
\dot\rho_{33}(t) &= -\frac{i}{2}\Omega_{23}(t)\cdot\rho_{32}(t) + \frac{i}{2}\Omega_{32}(t)\cdot\rho_{23}(t) - 2\big(A_{32} + A_{34} + \gamma_{\text{i}}(t)\big)\\
&\quad\cdot\rho_{33}(t),\\
\dot\rho_{44}(t) &= 2\big(A_{34}\cdot\rho_{33}(t) - A_{41}\cdot\rho_{44}(t)\big),\\
\dot\rho_{\text{ion}}(t) &= 2\gamma_{\text{i}}(t)\cdot\rho_{33}(t),
\end{aligned} \tag{1}$$

with $\text{Im}(\rho_{ii}(t)) = 0\ \forall t$. $\gamma_{\text{i}}(t)$ is the non-resonant ionization rate, whereas A_{ji} and $\Omega_{ij}(t)$ represent the decay rate (or *Einstein A-value*) of the $i \to j$ transition and its Rabi frequency, expressing the oscillation frequency of the probability amplitudes of the two states. $\Omega_{ji}(t) \equiv \Omega^*_{ij}(t)$, although in this study the Rabi frequencies are real (see below). The equations for the non-diagonal matrix elements, namely the quantum coherences, read instead:

$$\begin{aligned}
\dot\rho_{12} &= \frac{i}{2}\Omega_{12}(t)\cdot\big(\rho_{22}(t) - \rho_{11}(t)\big) - \frac{i}{2}\Omega_{32}(t)\cdot\rho_{13}(t)\\
&\quad + \left(i\Delta_1 - A_{21} - A_{32} - 2\gamma_{\text{L1}}\frac{\beta_1^2}{\Delta_1^2 + \beta_1^2}\right)\rho_{12}(t),\\
\dot\rho_{23} &= \frac{i}{2}\Omega_{23}(t)\cdot\big(\rho_{33}(t) - \rho_{22}(t)\big) - \frac{i}{2}\Omega_{21}(t)\cdot\rho_{13}(t)\\
&\quad + \left(i\Delta_2 - A_{21} - A_{32} - \gamma_{\text{i}}(t) - 2\gamma_{\text{L2}}\frac{\beta_2^2}{\Delta_2^2 + \beta_2^2}\right)\rho_{23}(t),\\
\dot\rho_{13} &= \frac{i}{2}\Omega_{12}(t)\cdot\rho_{23}(t) - \frac{i}{2}\Omega_{23}(t)\cdot\rho_{12}(t)\\
&\quad + \left(i(\Delta_1 + \Delta_2) - A_{21} - A_{32} - \gamma_{\text{i}}(t) - 2\gamma_{\text{L1}}\frac{\beta_1^2}{\Delta_1^2 + \beta_1^2} - 2\gamma_{\text{L2}}\frac{\beta_2^2}{\Delta_2^2 + \beta_2^2}\right)\\
&\quad\times\rho_{31}(t)
\end{aligned} \tag{2}$$

and $\dot\rho_{ji}(t) = \dot\rho^*_{ij}(t)$. γ_{Li} and Δ_i are the Lorentzian bandwidth of the ith laser and its detuning from the resonant frequency required by the transition, while β_i is the Lorentzian cut-off according to the phase-diffusion model (Zoller and Lambropoulos, 1979; Lambropoulos and Lyras, 1989). In the $\Delta_i \ll \beta_i$ limit, the terms with β_i reduce to $2\gamma_{\text{Li}}$; conversely, when $\Delta_i \gg \beta_i$, the same terms become negligible and the laser appears monochromatic.

The Rabi frequency can be calculated as (Suryanarayana and Sankari, 2023; Sankari et al., 2008; Bushaw et al., 1999)

$$\Omega^{\text{even}}_{ij}(t) = 2\sqrt{\frac{3gA_{ji}\lambda^3 p(t)}{8\pi hc}}\cdot\begin{pmatrix} J & 1 & J'\\ -m & q & m'\end{pmatrix} \tag{3}$$

for even–even isotopes and

$$\Omega^{\text{odd}}_{ij}(t) = 2\sqrt{\frac{3gA_{ji}\lambda^3 p(t)}{8\pi hc}\cdot(2F+1)(2F'+1)}\cdot\begin{Bmatrix} J & F & I\\ F' & J' & 1\end{Bmatrix} \tag{4}$$

otherwise. In Eqs. (3) and (4), g is the degeneration of the upper level, $p(t)$ identifies the power density of the laser, $q = 0$ and $|q| = 1$ determine linear and circular polarization (in this case it is linear), $()$ and $\{\}$ are the Wigner 3-j and 6-j symbols and λ is the laser wavelength. Inside these symbols, J and I are the quantum numbers for the absolute

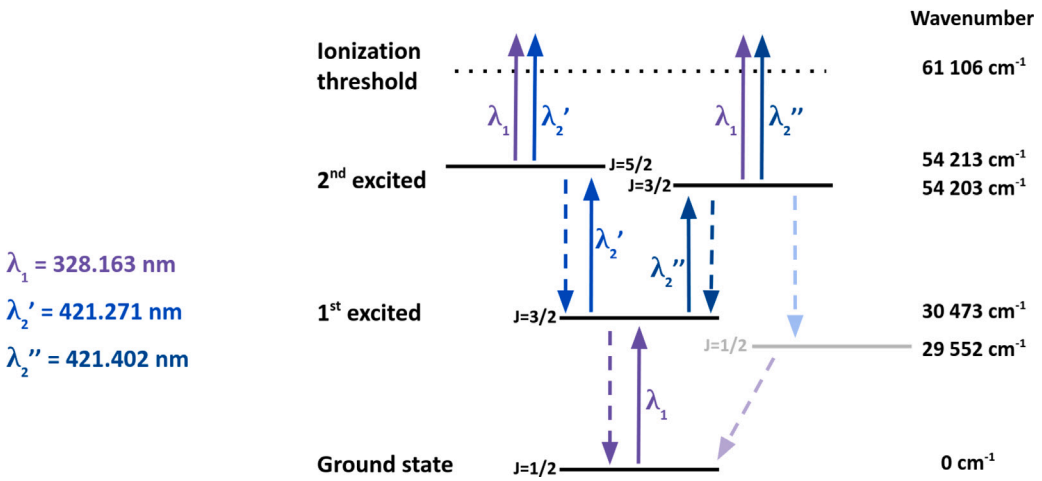

Fig. 1. Ionization paths used for silver: scheme 1 involves the 2nd excited level with $J = 5/2$, while scheme 2 exploits the one with $J = 3/2$.

values of the orbital angular momentum and of the nuclear spin, m is the magnetic angular momentum quantum number and F represents the hyperfine quantum number, *i.e.*, the absolute value of the total angular momentum $\vec{F} \equiv \vec{I} + \vec{J}$. In our notation, the primed quantum numbers refer to the upper level, while the non-primed refer to the lower. Finally, the non-resonant ionization rate is defined as

$$\gamma_i(t) \equiv \sigma\Phi(t) = \sigma \cdot \frac{\lambda}{hc} \cdot p(t), \tag{5}$$

with σ and $\Phi(t)$ being the cross section of the process and the photon flux of the ionizing laser. From Eq. (5) we can see that, for a given power of the laser, $\gamma_i \propto \lambda$.

In this study, the excitation lasers are devoted to ionization as well, hence $\gamma_i(t)$ is the sum of two components. $p(t)$ is assumed to have a Gaussian shape, reflecting the time profile of the laser pulse. Unlike A_{ji}, $\Omega_{ij}(t)$ and $\gamma_i(t)$ depend on the power; therefore, for high intensity, a saturation of the excitation and ionization transitions can be reasonably expected, with the decay transitions losing relevance. A peculiarity of this system is that A_{ji} determines the decay rate, but also contributes to define the oscillation frequency between resonant levels, which is $\propto \sqrt{A_{ji}p(t)}$. On the other hand, the non-resonant ionization rate is more sensitive to $p(t)$, since it has a linear dependence. For this reason, the condition with a 3rd laser exclusively devoted to non-resonant ionization is also analyzed.

In general, also other processes, such as collisions, can lead to excitation, de-excitation and ionization of the states; however, a previous study (Mariotti, 2024) showed that these mechanisms have negligible interaction rates under the experimental conditions examined. In particular, the collisional rate expected online, $10^4 \div 10^5$ s^{-1}, is much lower than the A-values of the excited states, therefore it is difficult for other levels to be significantly populated in this way.

Another theoretical tool adopted in this work, for the estimation of the isotopic abundances present in the SPES LIS after a typical irradiation cycle, are Bateman's equations (Bateman, 1910). Such equations describe the dynamics of a chain of radioactive nuclei; in particular, the variation of the number of nuclei of the nth nucleus of the chain corresponds to

$$\dot{N}_n(t) = \kappa_{n-1}N_{n-1}(t) - \kappa_n N_n(t) + R_n, \tag{6}$$

where κ_n is its radioactive disintegration constant and R_n is its production rate excluding the radioactive decay contribution. In our case, R_n expresses ISOL in-target production, which can be simulated through Monte Carlo codes like FLUKA (Battistoni et al., 2015). This kind of differential system has an analytical solution, given by

$$N_n(t) = \sum_{i=0}^{n}\left[\left(\prod_{j=1}^{n-1}\kappa_j\right) \cdot \frac{\kappa_j N_i(0) \cdot e^{-\kappa_j t} + R_i(1 - e^{-\kappa_j t})}{\prod_{k=i,k\neq j}^{n}(\kappa_k - \kappa_i)}\right]. \tag{7}$$

Table 1
Model parameters used to reproduce the SPES online experimental configuration.

Parameter	Value	Source
λ_1	328.163 nm	Khwairakpam et al. (2023)
λ_2 (Scheme 1)	421.271 nm	Khwairakpam et al. (2022)
λ_2 (Scheme 2)	421.402 nm	Khwairakpam et al. (2023)
β_i	$8 \cdot \gamma_{Li}$	
ρ	1.55 mm	Khwairakpam (2023)
τ_{FWHM}	30 ns	Scarpa et al. (2022)
T	$3 \cdot \tau_{FWHM}$	
A_{21}	1.380×10^8 s^{-1}	Smith et al. (2001)
A_{32} (Scheme 1)	2.606×10^7 s^{-1}	Smith et al. (2001)
A_{32} (Scheme 2)	4.362×10^6 s^{-1}	Smith et al. (2001)
A_{34}	2.311×10^7 s^{-1}	Smith et al. (2001)
A_{41}	1.223×10^8 s^{-1}	Smith et al. (2001)
σ	10^{-18} cm^2	

3. Results and discussion

Table 1 reports all the model parameters used to study the two ionization schemes chosen for silver in the SPES online configuration. In particular, τ_{FWHM} and T are the Full Width at Half Maximum (FWHM) of the Gaussian laser pulse and its total duration, while ρ represents the radius of the laser spot which maximizes the interaction volume in the LIS. The Rabi frequencies of all possible transitions are calculated using the Wigner coefficients and then averaged, whereas the Einstein coefficients are taken from a computational database (Smith et al., 2001). The order of magnitude of σ is decided on the basis that, in experimental practice, commercial lasers cannot saturate the non-resonant transitions. β_i and T are chosen in such a way as not to neglect important information in the tails of the Lorentzian and Gaussian distributions. The photo-ionization of ^{111}Ag is investigated by varying the average power and the Lorentzian linewidth of the lasers. The time-resolved power of a pulse can be expressed using a Gaussian distribution:

$$P(t) = P_0 \cdot \exp\frac{-(t - T/2)^2}{2\sigma_G^2}, \tag{8}$$

with P_0 being the power peak and $\sigma_G \approx \tau_{FWHM}/2.355$. Dividing by the beam section $\pi\rho^2$, the power density $p(t)$ can be easily obtained. The average power emitted by the laser device can be then identified by

$$\bar{P} = r \cdot \int_0^{\frac{1}{r}} p(t)dt \approx r \cdot \int_{-\infty}^{+\infty} p(t)dt = r\sqrt{2\pi}\sigma_G P_0, \tag{9}$$

where r is the pulse rate. Finally, when calculating the ionization efficiency, the intrinsic contribution of the physical process is multiplied

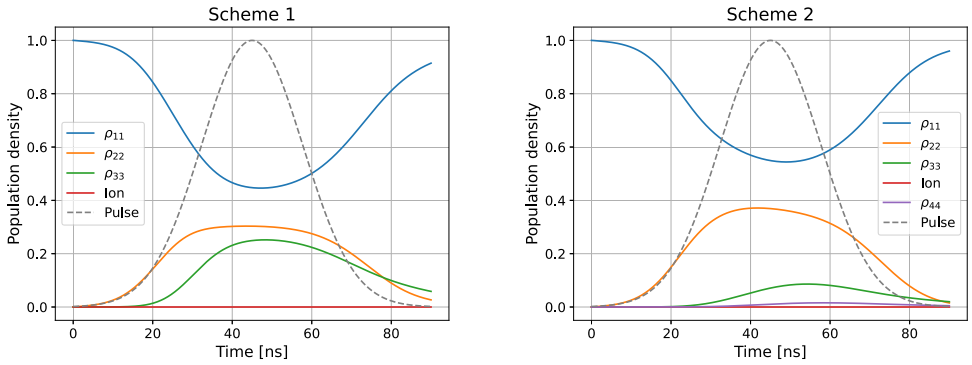

(a) Population densities before saturation ($\bar{P}_i = 1\,\text{mW}$).

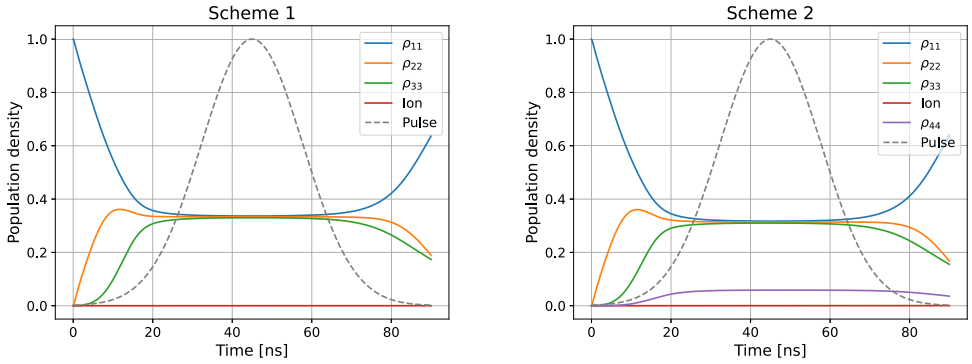

(b) Population densities corresponding to the saturation powers of the two schemes ($\bar{P}_1 = 50\,\text{mW}$, $\bar{P}_2' = 20\,\text{mW}$, $\bar{P}_2'' = 200\,\text{mW}$).

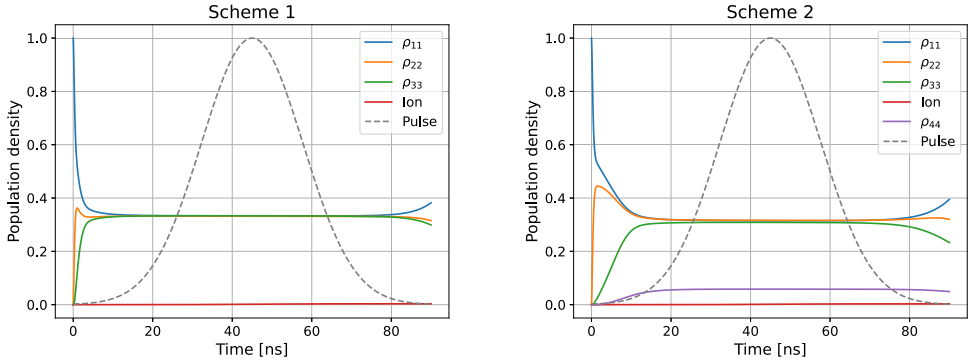

(c) Population densities obtainable using the excitation lasers at high power ($\bar{P}_i = 1\,\text{W}$).

Fig. 2. Level population densities of the two schemes studied under different conditions; the laser bandwidth is always $\gamma_{\text{Li}} = 6$ GHz, and the pulse shape normalized to 1 is overlapped to the curves.

by a factor $\eta = 0.2$, expressing the ratio between the laser interaction volume and the SPES LIS volume (Khwairakpam et al., 2024b,a).

3.1. Population densities

The ionization efficiency is studied setting $\Delta_i = 0$, $\gamma_{\text{Li}} = 6$ GHz and varying the average power in the range between 10 μW and 10 W, which is the highest order of magnitude achievable by the online laser system (Scarpa et al., 2022). First of all, the density matrix is used to study the saturation of the resonant transitions. To do this, the saturation power of the 1st transition is defined as the minimum 1st laser power required to obtain two equal populations of ground state and 1st excited state. Similarly, when the 1st transition is saturated, the saturation power of the 2nd transition corresponds to the minimum 2nd laser power which produces three equal populations of ground state, 1st excited and 2nd excited. In the present work, populations are considered "equal" when their difference is within 0.5% at $T/2$.

The saturation values found in this analysis are $\bar{P}_1 = 50$ mW for the 1st transition, $\bar{P}_2' = 20$ mW for the 2nd transition of scheme 1 and $\bar{P}_2'' = 200$ mW for the 2nd transition of scheme 2; the last one is the highest, also due to the decay toward the non-resonant level. The level populations related to these values are depicted in Fig. 2(b): what emerges is that the transition-saturation powers are still too low to obtain a consistent ionization. In detail, ion populations of 0.01% and 0.04% are obtained by the two schemes, with scheme 2 looking better only because the saturation of its 2nd step requires higher power. Pushing the power of both lasers up to 1 W, ion populations of 0.3% are achieved (Fig. 2(c)). For comparison, an example below saturation, using $\bar{P}_i = 1$ mW, is also shown (Fig. 2(a)). All graphs are equipped with the pulse profile normalized to 1: with high power, one can see

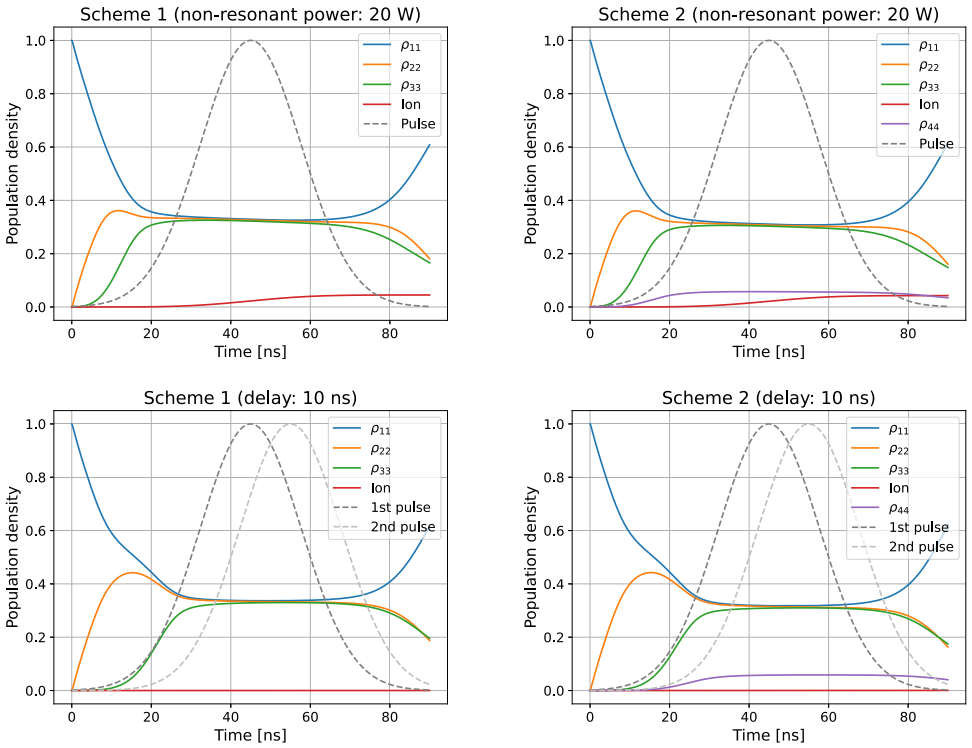

Fig. 3. Population densities corresponding to the transition-saturation powers of the two schemes with the addition of a 20 W non-resonant laser (upper graphs) and with a 10 ns delay between the laser pulses (lower graphs); the pulse shape normalized to 1 is overlapped to the curves; $\bar{P}_1 = 50$ mW, $\bar{P}_2' = 20$ mW, $\bar{P}_2'' = 200$ mW, $\gamma_{Li} = 6$ GHz.

that excited levels are populated already by the photons in the Gaussian left tail.

To improve these values, a laser exclusively devoted to non-resonant ionization should be used. An example is shown in the upper graphs of Fig. 3, where in saturation regime a non-resonant 20 W green laser (532 nm) enhances the ion population up to 4.5% and 4.3% for the two schemes. Setting 30 W, values as high as 6.7% and 6.3% are found. It can be noticed that, under these conditions, the equilibrium becomes transient, as the non-resonant step continuously removes atoms from the resonant system.

Finally, the effect of a time delay applied between the two pulses is also studied, but it turns out that the best configuration is without any offset. An example, computed with a delay of 10 ns, is shown in the lower graphs of Fig. 3: in this case, the 2nd transition saturates later and the ions produced are slightly less.

3.2. Efficiency optimization

The previously defined volume factor η is now applied to the population densities to mimic the experimental conditions more faithfully. It is important to note that the resulting efficiency is only related to the physical interactions within one pulse of the lasers. To obtain the overall efficiency of the LIS, this value has to be integrated in time, together with the pulse rate, the atom flux from the target, the loss rate implied by the thermal-mechanical properties of the system and the radioactive decay. We can think of a simple differential equation considering the atom flux ϕ, the photo-ionization efficiency ε, the radioactive decay constant κ and a loss factor l to express the amount of the non-ionized nuclide of interest in the LIS:

$$\dot{N}(t) = \phi - \varepsilon r N(t) - l N(t) - \kappa N(t), \tag{10}$$

whose solution for $N(0) = 0$ is

$$N(t) = \frac{\phi}{\varepsilon r + l + \kappa}[1 - \mathrm{e}^{-(\varepsilon r + l + \kappa)t}]. \tag{11}$$

Given that in a state-of-the-art ion source atoms survive around 10^{-3} s before being lost, we can suppose $l = 10^3$ s^{-1}. On the other hand, for medical radionuclides, which are expected to live at least a few days, $\kappa \sim 10^{-6}$ s^{-1}: the radioactive term is thus negligible. Therefore, εr has to compete with l to obtain a satisfactory ion yield: considering $r = 10$ kHz available at SPES, we can say that the ionization term is not negligible with respect to the loss term if at least $\varepsilon > 10^{-3}$ (or 0.1%).

The ionization efficiency as a function of the average power of the two lasers can be visualized in the 2D power maps of the two schemes depicted in Fig. 4 (upper graphs). Efficiency is generally optimized at high power, as can be expected. If both lasers operate at more than 1 W, both schemes give an overall efficiency between 0.1% and 0.7%, with a small advantage for scheme 1. However, one can notice that, in both schemes, the efficiency is more affected by the second laser power. In detail, if $\bar{P}_2 = 5 \div 10$ W, even with first laser power down to $\bar{P}_1 = 1$ mW, a 0.1% efficiency can be recovered. Conversely, if $\bar{P}_1 = 5 \div 10$ W, the 2nd must work at least at $\bar{P}_2 = 10$ mW for scheme 1 and $\bar{P}_2 = 100$ mW for scheme 2. In general, with high pulse rate, both schemes are good if the second laser can operate at high power, while scheme 1 turns out to be better if the first laser is preferred to work at high power.

In the lower graphs of Fig. 4, the same situation is represented with the addition of a 20 W non-resonant green laser (the logarithmic scale is removed for better visualization). Now, the maximum efficiency is enhanced to nearly 1.6%, but in general values higher than 0.1% are achievable even if the excitation lasers do not push to their limit. When the latter overcome the saturation power, the increase from 0.7% to 1% is very slow and almost looks like a *plateau*; subsequently, when they approach 10 W, their contribution to the third step becomes relevant and the slope is again steep.

A suppression of efficiency can be observed when the 1st laser exceeds the saturation threshold and the 2nd operates at low power. This phenomenon can be explained by the high value reached by the Rabi frequency of the 1st transition (up to 380 GHz at 10 W) with respect to the 2nd, which is smaller at equal power since $A_{21} > A_{32}$

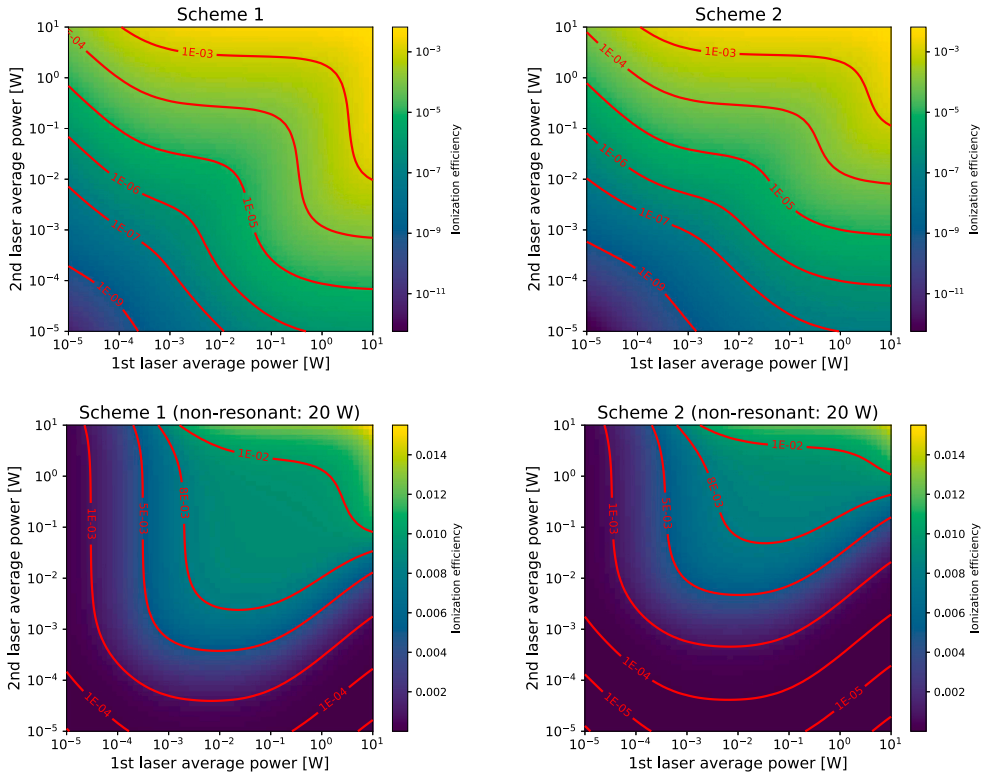

Fig. 4. Upper graphs: power maps expressing the ion yield as a function of the average power of the two lasers for scheme 1 (left) and scheme 2 (right) with $\gamma_{Li} = 6$ GHz; lower graphs: same with the addition of a 20 W non-resonant laser for the third step.

in both schemes. The $\Omega_{12} \gg \Omega_{23}$ limit leads to a dramatic increase in quantum oscillations between the ground state and the 1st excited level, resulting in an obstacle for the 2nd step. In other words, the 1st excited is more likely to undergo stimulated emission by interacting with the 1st laser than to be further excited by the 2nd laser. This effect is less noticeable without the non-resonant laser, since under those conditions the ionization process depends too strictly on the power of the 1st laser.

Finally, the same trend is visible from another perspective in the plots of Fig. 5, where each laser power is fixed to its saturation value and the efficiency as a function of the other laser is studied, varying the power of the non-resonant laser.

3.3. Broadening effects

The current paragraph aims to provide a concise discussion on two broadening mechanisms which can affect the physical process under study: power broadening and Doppler broadening. Concerning the former, if the saturation power P_{sat} and the natural linewidth γ_{nat} of the transition are known, using the formula

$$\mathrm{FWHM_p} = 2\gamma_{nat}\sqrt{1 + P/P_{sat}} = \frac{A_{ji}}{2\pi}\sqrt{1 + P/P_{sat}} \tag{12}$$

it is possible to calculate the broadening of the Lorentzian profile caused by the laser power (Letokhov, 1987). From the plot in Fig. 6, it is clear that the transition with the lowest saturation power is the most affected by power broadening. However, even at high power, the maximum registered broadening is only 0.3 GHz: for this reason, it can be safely stated that our system will not be affected if $\gamma_{Li} > 1$ GHz is used.

Another important effect to take into account is Doppler broadening. The broadened FWHM can be expressed by the formula (Letokhov, 1987)

$$\mathrm{FWHM_D} = \frac{1}{\lambda}\sqrt{\frac{8k_B T \ln 2}{m}}, \tag{13}$$

which is sensitive to the absolute temperature of the environment and the average mass of the constituents of the system. In the SPES configuration, the temperature of the target-ion source unit is kept at 2000 ° C, to favor the diffusion and effusion processes of the exotic species produced in the target box. Regarding the mass of the atoms in the LIS, according to FLUKA simulations performed (Ballan et al., 2020) in the context of the ISOLPHARM project, the average mass number of the products of a UC_x target irradiated with 40 MeV protons at 200 μA is $A = 115$, with a general production ranging from $A \sim 70$ to $A \sim 160$. Under these assumptions, it turns out that, for the two transitions, $\mathrm{FWHM_{D1}} = 3.0$ GHz and $\mathrm{FWHM_{D2}} = 2.3$ GHz. This means that using $\gamma_{Li} = 6$ GHz for both lasers, as done up to now, the number of ions lost due to the Doppler effect is negligible. It must be noted that this bandwidth has been chosen as a reference in these calculations since it is easily reachable by the SPES online lasers with the use of one etalon (Scarpa et al., 2022); nevertheless, sharper bandwidths, if compliant with the limits imposed by the broadening effects, are likely to improve the efficiency.

3.4. Isotopic selectivity

Moving to isotopic selectivity, let us focus first on ^{111}Ag, whose nuclear spin is the same as the stable silver isotopes: $I = 1/2$. According to the literature, odd-even silver isotopes with this nuclear spin are characterized by hyperfine shifts of 3 GHz or less, while for ^{111}Ag mass and field shifts combined do not exceed 0.5 GHz (Jading et al., 1997): again, $\gamma_L = 6$ GHz should be enough to include atoms with a shift of this size. In this work, for simplicity, the resonance frequency is set at the center of the hyperfine splitting; anyway, in the presence of new spectral data, it could be possible to tune the laser directly on the most efficient line and, doing so, improve the ion yield.

Another study of interest for ISOLPHARM may regard the separation of ^{111}Ag from its most likely isotopic contaminant, namely ^{112}Ag. The latter, an odd-odd isotope, has an integer nuclear spin of $I = 2$. As

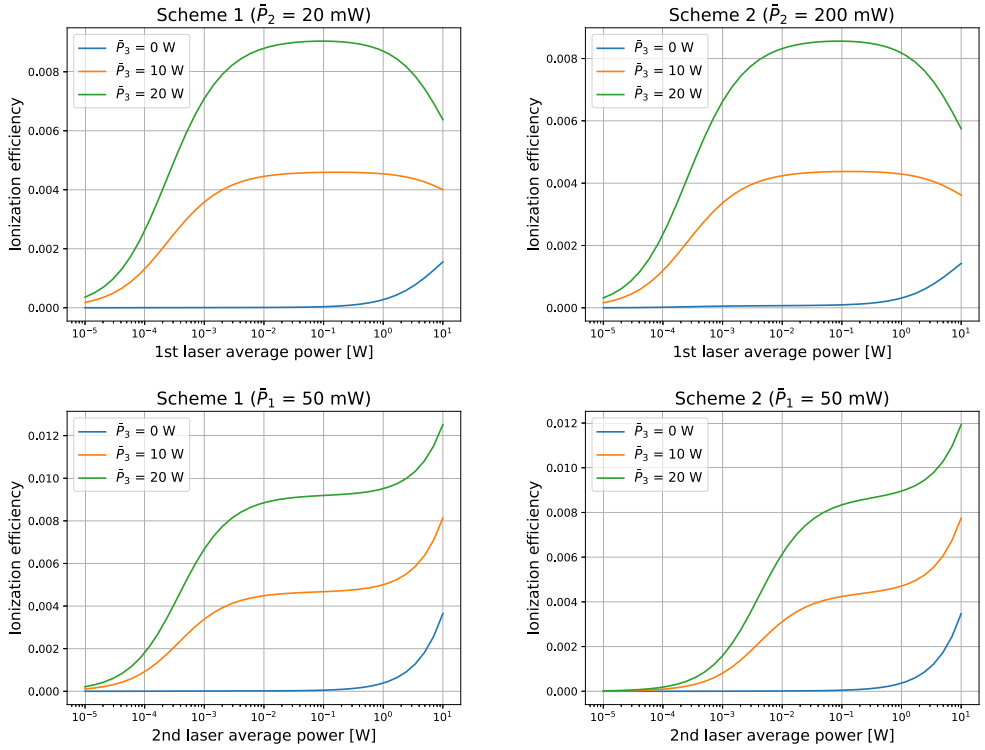

Fig. 5. Ionization efficiency curves of the two schemes using one excitation laser at saturation power, varying the other one and adding a non-resonant ionizing laser with different power ($\bar{P}_3$); γ_{Li} = 6 GHz.

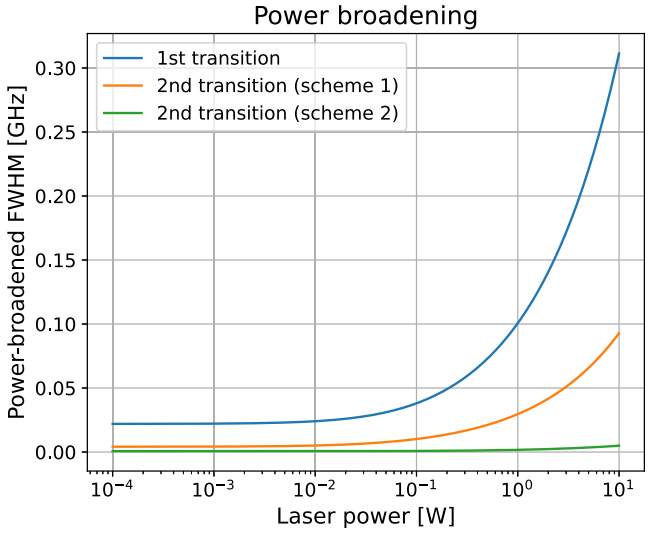

Fig. 6. Power broadening of the Lorentzian FWHM of the resonant transitions calculated using γ_{Li} = 6 GHz and the saturation powers determined in Section 3.1: $\bar{P}_1$ = 50 mW, $\bar{P}_2'$ = 20 mW and $\bar{P}_2''$ = 200 mW.

reported in the literature, neutron-rich isotopes of silver with even mass number usually feature a larger hyperfine splitting; for example, a recent study dealing with A = 114 to A = 120 Ag isotopes revealed several shifts in the region between 10 GHz and 20 GHz (Van den Borne et al., 2025). A preliminary evaluation can be performed hypothesizing a shift in this range of frequency.

To have a realistic idea of the expected abundances of these silver isotopes in the SPES ion source, the scenario after a typical 6 h irradiation cycle with a 40 MeV, 200 μA proton beam impinging on a UC_x target can be simulated. In particular, the SPES UC_x target is made of 7 disks with thickness 0.8 mm, properly spaced in order to obtain a uniform temperature in the target box. With reference to Eq. (6), the decay constants of the two isotopes are $\kappa^{Ag_{111}} = 1.077 \times 10^{-6}$ s^{-1} and $\kappa^{Ag_{112}} = 6.151 \times 10^{-5}$ s^{-1}, whereas production rates $R^{Ag_{111}} = 6.1 \times 10^{8}$ s^{-1} and $R^{Ag_{112}} = 2.9 \times 10^{9}$ s^{-1} are taken from the ISOLPHARM database of FLUKA in-target calculations (Andrighetto et al., 2019; Ballan et al., 2020). Inserting these values in Bateman's equations, abundances of a_{111} = 0.842 and a_{112} = 0.158 are estimated under these conditions (Mariotti, 2024). Such calculations take into account the contribution of the radionuclide precursors in the SPES target: in detail, the decay chains with ^{111}Pd and ^{112}Pd are considered ($\kappa^{Pd_{111}} = 4.940\times10^{-4}$ s^{-1}, $\kappa^{Pd_{112}} = 9.151\times10^{-6}$ s^{-1}, $R^{Pd_{111}} = 1.3\times10^{10}$ s^{-1} and $R^{Pd_{112}} = 4.1 \times 10^{10}$ s^{-1}), while the nuclides with more neutrons, characterized by much shorter lifetimes, are assumed to instantly decay into Pd.

As our selectivity index, we can define the degree of enrichment for the isotope ^{111}Ag:

$$\xi \equiv \frac{\varepsilon_{111} \cdot a_{111}}{\varepsilon_{111} \cdot a_{111} + \varepsilon_{112} \cdot a_{112}}, \tag{14}$$

where ε_i is the ionization efficiency of the isotope with mass number i. The behavior of ξ as a function of the laser power for hypothetic hyperfine shifts of 10 GHz and 20 GHz for the 1st step is shown in Fig. 7, where both schemes are used. The shifts are implemented in the model using the parameter Δ_1, while γ_{Li} has been lowered to 4 GHz to slightly improve the selectivity without losing too many ions. Although experimental data are lacking, the hyperfine shift of the 2nd jump should be smaller and is therefore neglected. From this qualitative analysis, we can say that, for a hyperfine shift of the 1st transition of ^{112}Ag below 10 GHz, a significant laser separation is extremely difficult to achieve under the experimental conditions examined. If, instead, the shift exceeds 20 GHz, a satisfactory degree of enrichment, ξ = 0.98, can be obtained by setting $\bar{P}_1 \sim 10$ μW. In general, it can be noted that isotopic selectivity cannot be achieved when $\bar{P}_1 > 100$ μW.

To maintain an acceptable efficiency, $\bar{P}_2$ can also be increased to 1 W. This would ionize just ∼ 0.001% of the atomic vapor in each pulse

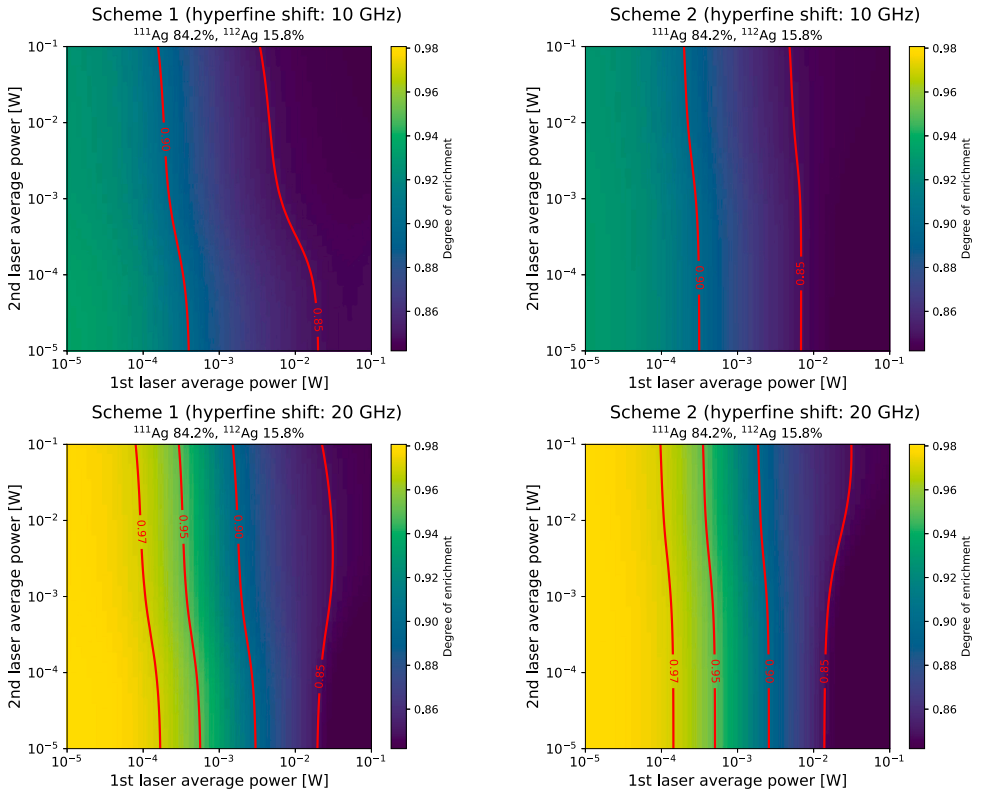

Fig. 7. Predicted degree of enrichment of ^{111}Ag in the SPES LIS for the two schemes with hypothetic hyperfine shifts 10 GHz and 20 GHz for ^{112}Ag; $\gamma_{Li} = 4$ GHz.

using only the excitation lasers. However, adding the non-resonant ionizing laser, this value could grow up to 0.04% — which is not much below the threshold set in Section 3.2 —, entailing an additional contribution to the radionuclidic purity of ^{111}Ag. As visible in the plots, the two schemes are almost equal for this kind of application.

4. Conclusions

Two silver laser photo-ionization schemes have been evaluated in terms of their ionization efficiency in the SPES ion source and their isotopic selectivity for ^{111}Ag, a radionuclide of medical interest for the ISOLPHARM project. A peculiarity of these schemes is the absence of a laser exclusively devoted to the non-resonant ionization step, which is operated by the excitation lasers themselves.

Regarding efficiency, a minimum acceptable value of 0.1% was chosen for the system under study. The main results are expressed by means of power maps (reported in Fig. 4): these are useful predictions suggesting the best combinations of laser power to optimize the ion yield while preserving photon economy. This information will be used in the next years, when the UC_x targets will be available at SPES and the ^{111}Ag production routine will have to be arranged. Even though the saturation powers of the resonant transitions are estimated in the range between 20 mW and 200 mW, a 0.1% to 0.7% ionization efficiency per pulse is obtained only when at least one of the two lasers operates at high power, namely > 1 W. For comparison, the impact of a dedicated non-resonant laser for the ionization step has been assessed. As an example, a 20 W green laser would reach a 0.1% efficiency already when the excitation lasers operate at saturation power, while almost 1.6% could be achieved at full power. In general, the two schemes behave similarly and are more sensitive (especially scheme 2) to the power of the second laser. The effect of a time delay between the two laser pulses has been investigated as well, revealing that the best condition is without any offset.

Broadening effects have also been studied. Without a non-resonant ionizing laser, power broadening cannot be avoided at the power needed to optimize the production of ions; however, its maximum effect — 0.3 GHz FWHM at 10 W for the 1st transition — is negligible with the laser bandwidths in use. Moreover, Doppler broadening has been estimated in the SPES target-ion source unit. The broadened FHWM values do not exceed 3 GHz, thus, with the 6 GHz nominal bandwidth of the SPES online lasers, the risk of losing ions for this reason is low.

The opportunity to perform isotopic selectivity between ^{111}Ag and the possible contaminant ^{112}Ag has also been investigated, with the aim of understanding whether the laser ion source can help to meet the medical authorities' requirements in terms of radionuclidic purity. In this case, the best results are obtained at low laser power. Since the hyperfine splitting of ^{112}Ag is not well known, shifts of 10 GHz and 20 GHz in the first transition were hypothesized and the consequent degree of enrichment was studied. This analysis took advantage of SPES online abundances predicted by means of FLUKA simulations and analytical equations accounting for the decay chains. The results say that, with a shift of 20 GHz and low power (~ 10 μW) and bandwidth (4 GHz) of the first laser, a degree of enrichment $\xi = 0.98$ could be reached by the LIS before mass separation. This approach causes an efficiency drop, with values around 0.001% achievable if the 2nd laser operates at 0.1 W. A non-resonant green laser would improve this efficiency up to 0.04%: in this case, thanks to the high pulse rate of 10 kHz ensured by the online laser system and to the long duration of the irradiation cycles, a satisfactory production could also be obtained when prioritizing selectivity.

In conclusion, the theoretical model proposed in this work provides interesting input parameters for the laser photo-ionization of ^{111}Ag. The same approach could also be applied to the ionization schemes of other radionuclides. In this framework, future experiments could help verify the findings of this study and refine the solidity of the predictions. In particular, the saturation powers could be tested experimentally,

together with the behavior of the ionization efficiency as a function of all the laser parameters. Finally, a precise investigation of the hyperfine structure of the radioisotopes of interest could be very useful to understand how to maximize the ion yield.

CRediT authorship contribution statement

Alberto Arzenton: Writing – original draft, Software, Methodology, Investigation, Formal analysis, Conceptualization. **Emilio Mariotti:** Writing – review & editing, Supervision. **Daniele Scarpa:** Writing – review & editing, Supervision. **Omorjit Singh Khwairakpam:** Writing – review & editing, Supervision. **Piergiorgio Nicolosi:** Writing – review & editing, Supervision. **Davide Serafini:** Writing – review & editing, Visualization. **Leonardo Mariotti:** Software, Investigation. **Alberto Andrighetto:** Resources, Project administration, Funding acquisition.

Declaration of competing interest

The authors declare that they have no known competing financial interests or personal relationships that could have appeared to influence the work reported in this paper.

Acknowledgments

This research is part of the SPES-ISOLPHARM project and of the experiment SPES_MED, supported by the Italian INFN.

Data availability

Data will be made available on request.

References

Andrighetto, A., Tosato, M., Ballan, M., Corradetti, S., Borgna, F., Di Marco, V., Marzaro, G., Realdon, N., 2019. The ISOLPHARM project: ISOL-based production of radionuclides for medical applications. JRNC 322, 73–77. http://dx.doi.org/10.1007/s10967-019-06698-0.

Arzenton, A., 2019. Studio dell'attività dei radionuclidi prodotti nel bersaglio SPES-ISOLPHARM (BSc Thesis). University of Padova.

Arzenton, A., 2023. Radiobiological model for β-emitter radiopharmaceutical therapy in dynamic cell cultures in the framework of the ISOLPHARM project. Il Nuovo Cimento C 46, 72. http://dx.doi.org/10.1393/ncc/i2023-23072-3.

Arzenton, A., Morselli, L., Lunardon, M., Russo, G., Andrighetto, A., 2022. A free Geant4 database of S-values for voxelized dosimetry of nonuniform activity distributions from PET/CT and SPECT/CT imaging. LNL Ann. Rep. 2021, 59.

Ballan, M., Tosato, M., Verona, M., Caeran, M., Borgna, F., Vettorato, E., Corradetti, S., Zangrando, L., Sgaravatto, M., Verlato, M., Asti, M., Marzaro, G., Mastrotto, F., Di Marco, V., Maniglio, D., Bisio, A., Motta, A., Quaranta, A., Zenoni, A., Pastore, P., Realdon, N., Andrighetto, A., 2020. Preliminary evaluation of the production of non-carrier-added ^{111}Ag as core of a therapeutic radiopharmaceutical in the framework of ISOLPHARM_Ag experiment. Appl. Radiat. Isot. 164, 109258. http://dx.doi.org/10.1016/j.apradiso.2020.109258.

Ballan, M., Vettorato, E., Morselli, L., Tosato, M., Nardella, S., Borgna, F., Corradetti, S., Monetti, A., Lunardon, M., Zenoni, A., Di Marco, V., Realdon, N., Andrighetto, A., 2021. Development of implantation substrates for the collection of radionuclides of medical interest produced via ISOL technique at INFN-LNL. Appl. Radiat. Isot. 175, 109795. http://dx.doi.org/10.1016/j.apradiso.2021.109795.

Balzer, M., Spiecker, F., Bluemel, S., Amthauer, H., Brenner, W., Spreckelmeyer, S., 2023. Evaluation of the ^{177m}Lu-concentration in in-house produced ^{177}Lu-radiopharmaceuticals and commercially available Lutathera®. EJNMMI Radiopharm. Chem. 8 (1), 37. http://dx.doi.org/10.1186/s41181-023-00222-2.

Bateman, H., 1910. The solution of a system of differential equations occurring in the theory of radioactive transformations. Math. Proc. Cambridge Philos. Soc. 15, 423–427.

Battistoni, G., Boehlen, T., Cerutti, F., Chin, P.W., Esposito, L.S., Fassò, A., Ferrari, A., Lechner, A., Empl, A., Mairani, A., Mereghetti, A., Garcia Ortega, P., Ranft, J., Roesler, S., Sala, P.R., Vlachoudis, V., Smirnov, G., 2015. Overview of the FLUKA code. Ann. Nucl. Energy 82, 10–18. http://dx.doi.org/10.1016/j.anucene.2014.11.007.

Bushaw, B., Nörtershäuser, W., Wendt, K., 1999. Lineshapes and optical selectivity in high-resolution double-resonance ionization mass spectrometry. Spectrochim. Acta Part B: At. Spectrosc. 54 (2), 321–332. http://dx.doi.org/10.1016/S0584-8547(98)00250-X.

EMA, 2022. https://www.ema.europa.eu/en/documents/product-information/pluvicto-epar-product-information_en.pdf.

Gramegna, F., the SPES collaboration, 2019. SPES, the LNL exotic beam ISOL facility. Il Nuovo Cimento C 42, 61. http://dx.doi.org/10.1393/ncc/i2019-19061-6.

Haken, H., Der Agobian, R., Pauthier, M., 1965. Theory of laser cascades. Phys. Rev. A 140, A437–A447. http://dx.doi.org/10.1103/PhysRev.140.A437.

Jading, Y., Catherall, R., Fedosseev, V.N., Jokinen, A., Jonsson, O.C., Kautzsch, T., Klöckl, I., Kratz, K.-L., Kugler, E., Lettry, J., Mishin, V.I., Ravn, H.L., Scheerer, F., Tengblad, O., Van Duppen, P., Walters, W.B., Wöhr, A., the ISOLDE Collaboration, 1997. Production of radioactive Ag ion beams with a chemically selective laser ion source. Nucl. Instrum. Methods Phys. Res. B 126, 76–80. http://dx.doi.org/10.1016/S0168-583X(96)01018-X.

Khwairakpam, O.S., 2023. Study, development and optimization of laser resonant photo-ionization processes applied to species of interest for the Isolpharm-SPES project (Ph.D. thesis). University of Siena.

Khwairakpam, O.S., Mancheva, R., Au, M., Bernerd, C., Centofante, L., Chrysalidis, K., Crepieux, B., Fedosseev, V.N., Heinke, R., Marchi, T., Mariotti, E., Marsh, B.A., Monetti, A., Nicolosi, P., Rothe, S., Scarpa, D., Schuett, M., Stora, T., Andrighetto, A., Manzolaro, M., 2024a. The SPES laser ion source: Time structure and laser enhancement measurements with Sm^+ beam. J. Phys.: Conf. Ser. 2743, 012066. http://dx.doi.org/10.1088/1742-6596/2743/1/012066.

Khwairakpam, O.S., Mancheva, R., Au, M., Bernerd, C., Centofante, L., Chrysalidis, K., Crepieux, B., Fedosseev, V.N., Heinke, R., Marchi, T., Mariotti, E., Marsh, B.A., Monetti, A., Nicolosi, P., Rothe, S., Scarpa, D., Schuett, M., Stora, T., Andrighetto, A., Manzolaro, M., 2024b. The SPES laser ion source: Time structure, laser enhancement and efficiency measurements with gallium at ISOLDE Offline 2. Nucl. Instrum. Methods Phys. Res. B 548, 165249. http://dx.doi.org/10.1016/j.nimb.2024.165249.

Khwairakpam, O.S., Mariotti, E., Scarpa, D., Nicolosi, P., Khanbekyan, A., Arzenton, A., Ferracane, S., Andrighetto, A., 2022. Laser photo-ionization study of ^{nat}Ag using opto-galvanic signal at SPES offline laser lab. JINST 17, C12009. http://dx.doi.org/10.1088/1748-0221/17/12/C12009.

Khwairakpam, O.S., Mariotti, E., Scarpa, D., Nicolosi, P., Khanbekyan, A., Ferracane, S., Arzenton, A., Andrighetto, A., 2023. Resonant laser ionization and fine-structure study of silver in an ablation plume. Appl. Sci. 13, 309. http://dx.doi.org/10.3390/app13010309.

Kiran Kumar, P.V., Sankari, M., Suryanarayana, M.V., 2003. Calculation of ^{91}Zr optical selectivities in two-color resonant three-photon ionization schemes. J. Opt. Soc. Am. B 20, 1807. http://dx.doi.org/10.1364/JOSAB.20.001807.

Lambropoulos, P., Lyras, A., 1989. Theory of resonant ionization by broad-band radiation in the determination of isotopic abundances. Phys. Rev. A 40, 2199. http://dx.doi.org/10.1103/PhysRevA.40.2199.

Letokhov, V.S., 1987. Laser Photoionization Spectroscopy, Academic Press, http://dx.doi.org/10.1016/B978-0-12-444320-4.X5001-8.

Mariotti, L., 2024. Studio della dinamica dei livelli atomici dell'argento-111 nell'interazione con radiazione laser per il progetto ISOLPHARM (BSc Thesis). University of Siena.

Morselli, L., Donzella, A., Arzenton, A., Asti, M., Bortolussi, S., Corradetti, S., D'Agostino, G., Di Luzio, M., Ferrari, M., Gandini, A., Lunardon, M., Villa, V., Salvini, A., Zangrando, L., Zenoni, A., Andrighetto, A., 2023. Production and characterization of ^{111}Ag radioisotope for medical use in a TRIGA Mark II nuclear research reactor. Appl. Radiat. Isot. 197, 110798. http://dx.doi.org/10.1016/j.apradiso.2023.110798.

Sankari, M., Kiran Kumar, P.V., Suryanarayana, M.V., 2008. Study of line shapes in the selective ionization of ^{176}Yb isotope in a two-step resonance, three-step ionization scheme. J. Opt. Soc. Am. B 25, 1820. http://dx.doi.org/10.1364/JOSAB.25.001820.

Scarpa, D., Mariotti, E., Khwairakpam, O.S., Parenti, V., Buono, A., Nicolosi, P., Calderolla, M., Khanbekyan, A., Ballan, M., Centofante, L., Corradetti, S., Lilli, G., Manzolaro, M., Monetti, A., Morselli, L., Andrighetto, A., 2022. New solid state laser system for SPES: Selective Production of Exotic Species project at Laboratori Nazionali di Legnaro. Nucl. Instrum. Methods Phys. Res. B 93, 083001. http://dx.doi.org/10.1063/5.0078913.

Serafini, D., Zancopè, N., Pavone, A.M., Benfante, V., Arzenton, A., Russo, V., Ballan, M., Morselli, L., Cammarata, F.P., Comelli, A., Russo, G., Scopelliti, F., Di Marco, V., Mastrotto, F., Asti, M., Maniglio, D., Sbarra, C., Bortolussi, S., Donzella, A., Zenoni, A., Gandini, A., Villa, V., Paderno, D., Zangrando, L., Corradetti, S., Mariotti, E., Salvini, A., Torrisi, F., Lunardon, M., Andrighetto, A., 2025. ^{111}Ag phantom images with Cerenkov Luminescence Imaging and digital autoradiography within the ISOLPHARM project. Appl. Radiat. Isot. 215, 111562. http://dx.doi.org/10.1016/j.apradiso.2024.111562.

Shore, B., 1990. The Theory of Coherent Atomic Excitation, Vol. 1 – Simple Atoms and Fields, Chap. 6, Wiley-Interscience.

Smith, P.L., Heise, C., Esmond, J.R., Kurucz, R.L., 2001. Atomic spectral line database from CD-ROM 23 of R. L. Kurucz. https://lweb.cfa.harvard.edu/amp/ampdata/kurucz23/sekur.html.

Suryanarayana, M.V., 2021. Isotope separation of ^{176}Lu a precursor to ^{177}Lu medical isotope using broadband lasers. Sci. Rep. 11, 6118. http://dx.doi.org/10.1038/s41598-021-85414-z.

Suryanarayana, M.V., 2022. Enrichment of ^{150}Nd for neutrinoless double-beta decay detection. Sci. Rep. 12, 11471. http://dx.doi.org/10.1038/s41598-022-15597-6.

Suryanarayana, M.V., 2023. Laser isotope separation of ^{223}Ra. Sci. Rep. 13, 7001. http://dx.doi.org/10.1038/s41598-023-34204-w.

Suryanarayana, M.V., Sankari, M., 2023. Laser isotope separation of ^{192}Ir. Appl. Radiat. Isot. 197, 110820. http://dx.doi.org/10.1016/j.apradiso.2023.110820.

Tosato, M., Asti, M., 2023. Lights and shadows on the sourcing of silver radioisotopes for targeted imaging and therapy of cancer: Production routes and separation methods. Pharm. 16, 929. http://dx.doi.org/10.3390/ph16070929.

Tosato, M., Asti, M., Dalla Tiezza, M., Orian, L., Häussinger, D., Vogel, R., Köster, U., Jensen, M., Andrighetto, A., Pastore, P., Di Marco, V., 2020. Highly stable silver(I) complexes with cyclen-based ligands bearing sulfide arms: A step toward silver-111 labeled radiopharmaceuticals. Inorg. Chem. 59, 10907–10919. http://dx.doi.org/10.1021/acs.inorgchem.0c01405.

Van den Borne, B., Stryjczyk, M., de Groote, R.P., Kankainen, A., Nesterenko, D.A., Ayoubi, L.A., Ascher, P., Beliuskina, O., Bissell, M.L., Bonnard, J., Campbell, P., Canete, L., Cheal, B., Delafosse, C., de Roubin, A., Devlin, C.S., Eronen, T., Ruiz, R.F.G., Geldhof, S., Gerbaux, M., Gins, W., Grévy, S., Hukkanen, M., Husson, A., Imgram, P., Koszorús, Á., Mathieson, R., Moore, I.D., Neyens, G., Pohjalainen, I., Reponen, M., Rinta-Antila, S., Vilen, M., Virtanen, V., Weaver, A.P., Zadvornaya, A., 2025. Binding energies, charge radii, spins, and moments: Odd-odd Ag isotopes and discovery of a new isomer. Phys. Rev. C 111, 014329. http://dx.doi.org/10.1103/PhysRevC.111.014329.

Vettorato, E., Morselli, L., Ballan, M., Arzenton, A., Khwairakpam, O.S., Verona, M., Scarpa, D., Corradetti, S., Caliceti, P., Di Marco, V., Mastrotto, F., Marzaro, G., Realdon, N., Zenoni, A., Donzella, A., Lunardon, M., Zangrando, L., Asti, M., Russo, G., Mariotti, E., Maniglio, D., Andrighetto, A., 2022. A new production method of high specific activity radionuclides towards innovative radiopharmaceuticals: the ISOLPHARM project. RAD Conf. Proc. 6, 8–14. http://dx.doi.org/10.21175/RadProc.2022.02.

Zoller, P., Lambropoulos, P., 1979. Non-Lorentzian laser lineshapes in intense field-atom interaction. J. Phys. B 12, L547. http://dx.doi.org/10.1088/0022-3700/12/18/003.